

FULL PAPER

Open Access



Examination of one-dimensional S-wave velocity structure using strong-motion data for high-seismic-intensity area during the 2018 Hokkaido Eastern Iburi earthquake

Naofumi Nakagawa^{1*} , Nobuo Takai¹  and Michiko Shigefuji²

Abstract

The Yufutsu Plain, a sedimentary basin surrounded by mountains, is located in the southern part of the Ishikari–Yufutsu Lowlands, Hokkaido, Japan. The Hidaka arc–arc collision zone, located in the eastern part of the Yufutsu Plain, forms the Hidaka Mountain range in central Hokkaido, with the Ishikari–Teichi–Toen Fault Zone of the Ishikari–Yufutsu Lowlands on the west side, which forms part of a major geological boundary that extends in the north–south direction. The 2018 Hokkaido Eastern Iburi earthquake (M_w 6.6) occurred at 03:08 JST on September 6, 2018, in this arc–arc collision zone. The K-NET HKD126 station in Mukawa Town, which is close to the severely damaged basin margin area, recorded strong-motion data with strong power for a predominant frequency of 0.5–1.0 Hz during the main shock. The peak ground acceleration was 661 cm/s^2 in the east–west direction. The site amplification characteristics of the shallow S-wave velocity structure, which was estimated from microtremor array observations and surface wave explorations, were one of the causes of this strong ground motion. It is essential to accurately estimate the depth of the seismic bedrock and basin margin to evaluate the long period of large earthquakes. In this study, we used strong-motion data recorded at HKD126 and three temporary strong-motion stations near the basin margin area to tune the deep S-wave velocity structure. First, we performed microtremor array observations and surface wave explorations to estimate the S-wave velocity structure to a depth of 1 km beneath the station at the hill site because a detailed shallow structure is not available for this site. Then, with a combination of the estimated S-wave velocity structure and the existing structure, we tuned the deep structures based on an autocorrelation function analysis using strong-motion data. The validity of the estimated structures from the shallowest depth to the seismic bedrock was verified based on the differences between the observed arrival time difference and theoretical travel time difference for the S-wave initial motion. We estimated the seismic bedrock of the four stations to be at a depth of 7–10 km. In addition, an autocorrelation function analysis suggests topological bedrock undulations.

Keywords 2018 Hokkaido Eastern Iburi earthquake, S-wave velocity structure, Temporary strong-motion observation, Autocorrelation function analysis, Microtremor array observation, Multi-channel analysis of surface waves

*Correspondence:

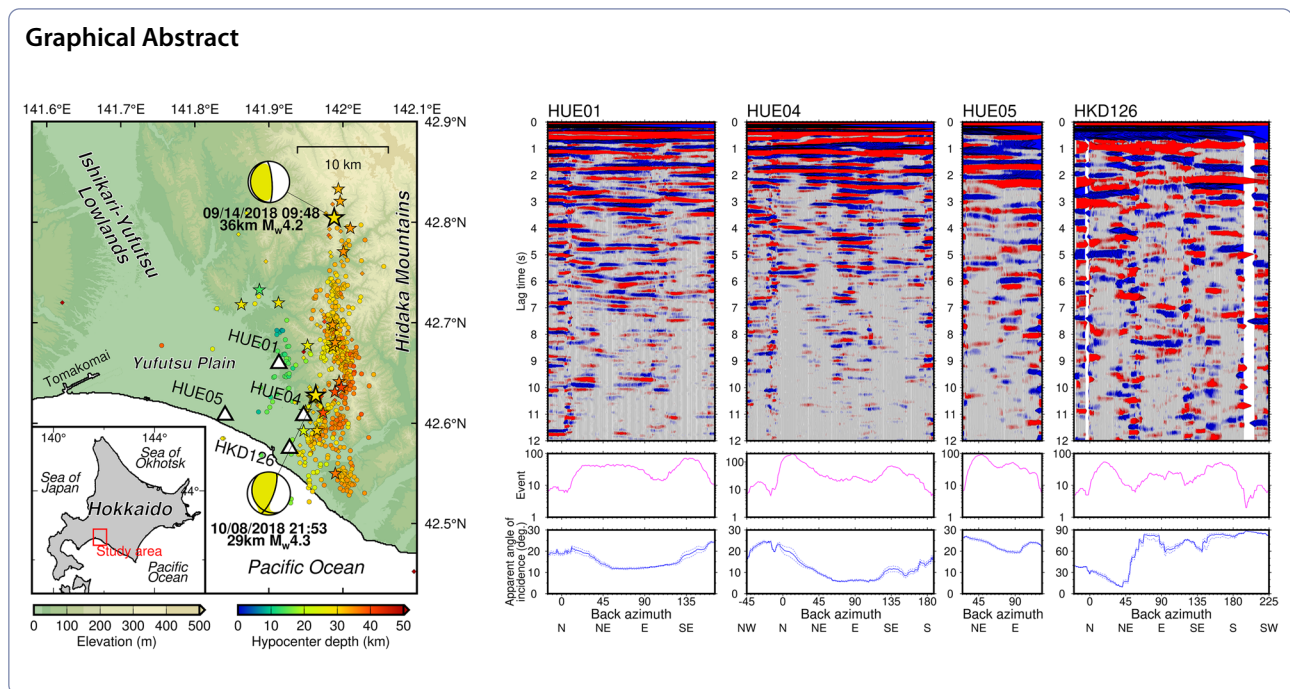
Naofumi Nakagawa

nakagawa.naofumi.e6@elms.hokudai.ac.jp

Full list of author information is available at the end of the article



© The Author(s) 2023. **Open Access** This article is licensed under a Creative Commons Attribution 4.0 International License, which permits use, sharing, adaptation, distribution and reproduction in any medium or format, as long as you give appropriate credit to the original author(s) and the source, provide a link to the Creative Commons licence, and indicate if changes were made. The images or other third party material in this article are included in the article's Creative Commons licence, unless indicated otherwise in a credit line to the material. If material is not included in the article's Creative Commons licence and your intended use is not permitted by statutory regulation or exceeds the permitted use, you will need to obtain permission directly from the copyright holder. To view a copy of this licence, visit <http://creativecommons.org/licenses/by/4.0/>.



Introduction

The Yufutsu Plain is located in the southern part of the Ishikari–Yufutsu Lowlands, Japan, with mountains to the east and west and the Pacific Ocean to the south. The plain is formed by the sedimentation of volcanic ash and fluvial alluvium and contains many marshes and peatlands (Ikeda et al. 1995). The Hidaka arc–arc collision zone, located in the eastern part of the Yufutsu Plain, forms the Hidaka Mountain range in central Hokkaido, with the Ishikari–Teichi–Toen Fault Zone of the Ishikari–Yufutsu Lowlands on the west side, which forms part of a major geological boundary that extends in a north–south direction (Iwasaki et al. 2004). The depth of the seismic bedrock with an S -wave velocity (V_S) of 3.0 km/s or more has been estimated to be around 8 km in the eastern part of the Yufutsu Plain, with the depth increasing in the eastward direction (Yoshida et al. 2007; NIED 2019c).

Serious strong ground motions that damage buildings have sometimes occurred on this plain. Long-period strong ground motions during the 2003 Tokachi-oki earthquake (M_w 8.0) caused fire damage to oil storage tanks in Tomakomai City, in the western Yufutsu Plain, 200 km west–northwest of the epicenter (Hatayama 2008). Using a V_S structure model based on microtremor array observations, Hatayama et al. (2007) concluded that the basin and seismic bedrock influenced the period of 7–8 s from numerical simulation and explained the cause of severe damage such as fire and sinking of floating roofs by the sloshing of the tanks. During the 2018 Hokkaido

Eastern Iburi earthquake (M_w 6.6) that occurred at 03:08 JST on September 6, 2018, the buildings damaged by the strong-motion were mainly concentrated in the center of Mukawa Town, 14.5 km south–southwest of the epicenter, which was located on the eastern edge of the Yufutsu Plain. The strong-motion data from the Mukawa strong-motion station (HKD126) of the Kyoshin Network (K-NET) operated by the National Research Institute for Earth Science and Disaster Resilience (NIED 2019b), indicated strong power that was able to destroy timber-frame buildings, with a peak ground velocity of over 100 cm/s. The main shock damaged an electric power plant (operated by the Hokkaido Electric Power Company) 23 km west of HKD126, which contributed to the blackout in Hokkaido.

Takai et al. (2019) concluded that the cause of the destructive strong-motion around Mukawa Town during the 2018 Hokkaido Eastern Iburi earthquake was the shallow V_S structures, as determined by microtremor array observations and surface wave explorations. The deep V_S structures have not been discussed in detail, even though large-sized microtremor array observations were also carried out (Takai et al. 2019). To verify and improve the deep V_S structures in the Yufutsu Plain for quantitative ground motion evaluation, these structures should be examined using a method that can detect deep structures.

In this study, autocorrelation function (ACF) analysis of the strong-motion data is used to tune the deep V_S structures around HKD126 and three temporary

strong-motion stations (Fig. 1a) located around the margin of the basin where the layer boundary is complex. In the ACF analysis, the shallow V_S structure is required for tuning the deep structure because the layer boundaries are tuned using the lag times for the reflected waves and the V_S values for each layer. We performed microtremor array observations and a multi-channel analysis of surface waves (MASW) and estimated the shallow V_S structure beneath a station for which there is no detailed V_S structure. Then, the deep V_S structure was tuned based on the ACF analysis results using small-magnitude records of the aftershocks recorded at strong-motion stations. Moreover, we examined the validity of the tuned V_S structures based on the differences between the theoretical travel time difference and observed arrival time difference of the S-wave initial motion.

Strong-motion stations

Temporary strong-motion observation stations were installed for approximately 1 to 3 months immediately after the main shock to determine the site amplification characteristics around the margin of the eastern Yufutsu Plain. In addition to HKD126, we used three temporary strong-motion stations HUE01, HUE04, and HUE05 around the target area installed by Takai et al. (2019). HUE04 is the same station as MKW01 in Takai et al. (2019). The instruments were overdamped moving coil-type accelerometers (Mitutoyo JEP-6A3 2 V/g) and data loggers (Hakusan DATAMARK LS-8800) with 24-bit 100 Hz sampling using 12 V load batteries. Table 1 shows the station information and Fig. 1a shows a location map of the stations and the epicenters of the events used for the analysis in this study. We selected strong-motion data at HKD126 from June 1, 1996, to May 31, 2022, and records that were extracted at each temporary station based on hypocenter information by Katsumata et al. (2019). HKD126 is at an altitude of 7 m. HUE04 was at an altitude of 24 m and was located 4 km north-northeast of HKD126. HUE05 was close to the power plant at an altitude of 3 m and was located 7.5 km west-northwest of HKD126. HUE01 was at an altitude of 22 m and was located 9.5 km north of HKD126. As an example of the seismic waveforms recorded at the four stations, Fig. 2 shows the acceleration waveforms for the transverse component and the spectrogram of the velocity waveforms, which were calculated by integrating the acceleration

waveforms, obtained from a multiple filter analysis (Dziwonski et al. 1969) of the event (M_w 4.3, depth: 32 km) on October 8, 2018. HUE04 recorded the smallest peak ground acceleration among the four stations even though HUE04 was the closest to the epicenter. Large S-wave amplitudes appeared at a frequency of around 2 Hz for HKD126 and HUE05 and around 7 Hz for HUE01 and HUE04, as shown in the spectrogram. The later phase at HUE05 and HKD126 also had large amplitudes.

According to the engineering geomorphologic classification (NIED 2019c; Wakamatsu and Matsuoka 2020), the HKD126 site is surrounded by a back marsh, delta and coastal lowlands, a natural levee, and an abandoned river channel. The HUE01 was at a terrace covered with volcanic ash soil, HUE04 was on a hill, and HUE05 was at a delta and coastal lowlands. These differences in geomorphology suggest a large variety of site amplification characteristics and velocity structures.

Shallow S-wave velocity structures

Microtremor array observations are widely conducted to investigate V_S structures in sedimentary basins and plains (e.g., Kudo et al. 2002; Özmen et al. 2017; Asano et al. 2022). MASW (Park et al. 1999) is commonly used to detect surface V_S structures. Takai et al. (2019) estimated V_S structures for HKD126 and HUE04 based on the microtremor array observations (radius=1–2000 m) and surface wave explorations. Tanaka et al. (2020) conducted microtremor array observations (radius=6–150 m) near HUE05 and a surface wave exploration on a nearby grass field to obtain phase velocities. Around HUE01, the detailed V_S structure is unknown at a depth shallower than the engineering bedrock. Therefore, we carried out microtremor array observations and a surface wave exploration at HUE01 to estimate the shallow V_S structure.

Microtremor array (small array: radius=8.66 and 17.32; large array: radius=200 m) observations were carried out beside HUE01 for half an hour and 0.6 km southwest of HUE01 for an hour on April 11, 2021, respectively (Fig. 1b). The seismometers were arranged in seven-station equilateral triangular arrays with a small radius and four-station equilateral triangular arrays with a large radius. We used servo-type velocity seismometers (Nanometrics Trillium Compact 20 s) with -3 dB points at 0.05 and 108 Hz, and 24-bit data loggers (Hakusan

(See figure on next page.)

Fig. 1 Location map of the study area. The top panel shows strong-motion stations and epicenters, and the bottom panel shows microtremor observation sites and a measurement line of surface wave exploration. **a** The circle denotes the epicenter of the aftershock determined by Katsumata et al. (2019), the diamond denotes the epicenter determined from the JMA (Japan Meteorological Agency) catalog and the star denotes the epicenter determined by F-net. Hokkaido and the study area (red rectangle) are shown in the inset. **b** The red circles and lines denote the microtremor array observation stations, and the blue line denotes the surface wave measurement line. The white triangles in the two maps denote the strong-motion stations used in this study

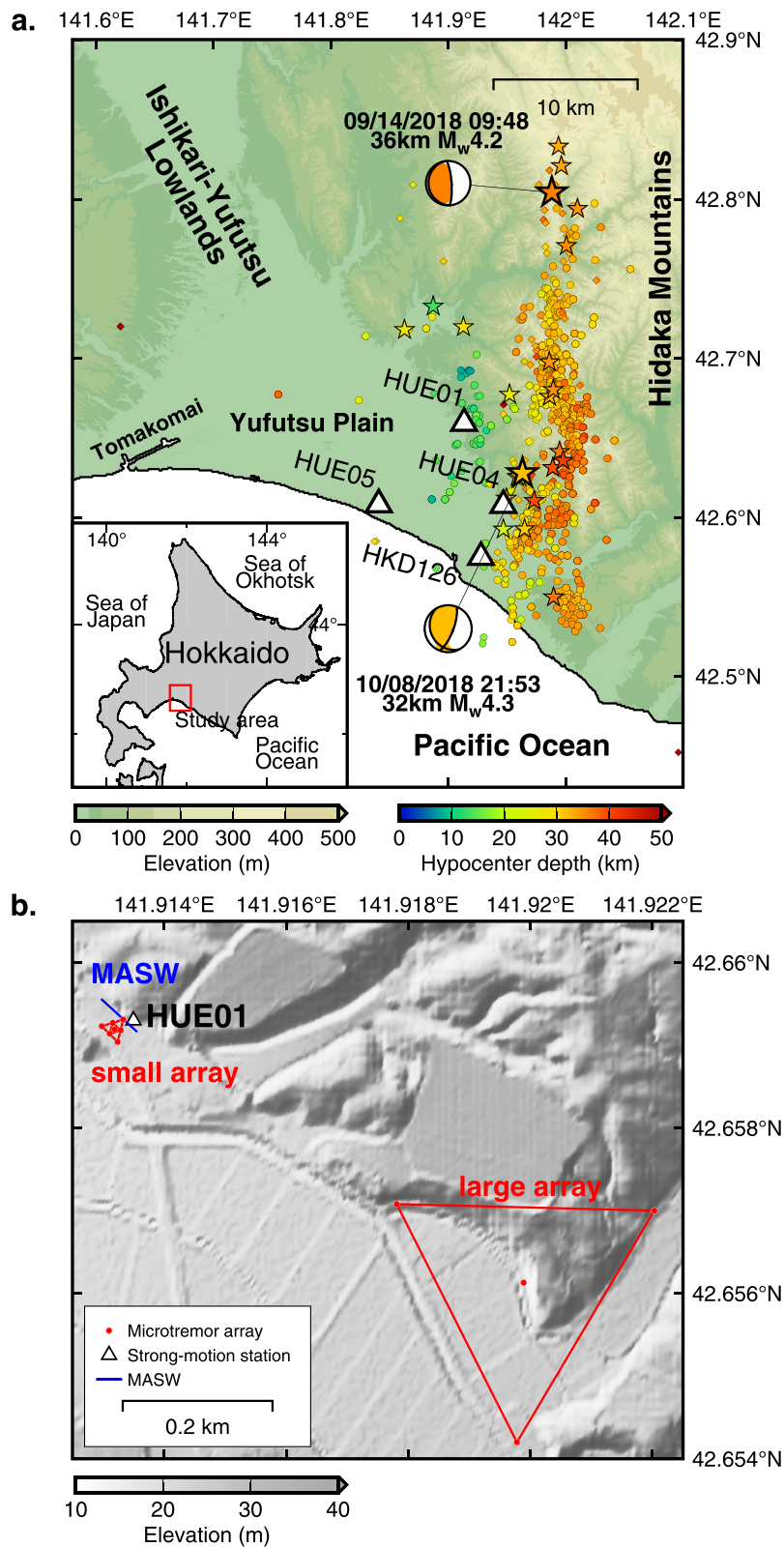


Fig. 1 (See legend on previous page.)

Table 1 Number of events recorded at each station and used for each analysis

Code	Latitude	Longitude	Altitude	Events	Analysis 1	Analysis 2	Observation period
HUE01	N42.6593°	E141.9135°	22 m	554	300	21	Sep. 10 to Oct. 15 2018
HUE04	N42.6077°	E141.9470°	24 m	895	532	–	Sep. 9 to Dec. 15 2018
HUE05	N42.6081°	E141.8409°	3 m	618	213	22	Sep. 10 to Nov. 26 2018
HKD126	–	–	–	272	272	25	–

Analysis 1 is an ACF analysis and Analysis 2 is an analysis of the differences between the arrival time difference and travel time difference using HUE04 as a reference site

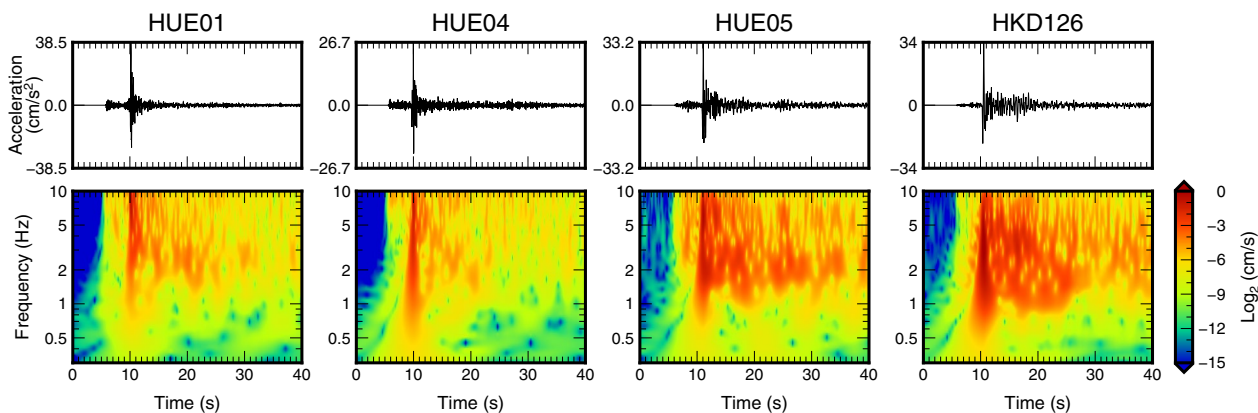


Fig. 2 Acceleration waveforms of the transverse component and the spectrogram of the velocity waveforms. The event (M_w 4.3, depth: 32 km) at 21:53 JST on October 8, 2018 was used for these acceleration waveforms. The spectrogram of their velocity waveforms, which were calculated by integrating the acceleration waveforms, was calculated using multiple filter analysis

DATAMARK LS-8800) set to a 200 Hz sampling rate with GPS time calibration. To stabilize the sensor, we attached a stainless pedestal, and the total weight was 6 kg. After the instruments were stable, the low-noise sections of the acquired data were used to examine the phase velocities for the Rayleigh waves using the spatial autocorrelation (SPAC) method (Okada 2003). We also carried out a surface wave exploration beside HUE01 on April 16, 2021. We set 24 geophones with a 4.5 Hz vertical component (Geospace) spaced 2 m apart and a Geode (Geometrics) and used an 8 kg wood hammer. The phase velocities for MASW were examined using the frequency-wavenumber method (Lacoss et al. 1969). The phase velocities determined using MASW in the high-frequency range were combined with those determined using the SPAC method in the low-frequency range. We obtained the phase velocities for the Rayleigh waves in the frequency range of 0.8–30 Hz. We also obtained the observed phase velocities for the Rayleigh waves (Tanaka et al. 2020). The observed phase velocities above 7 Hz were small and were excluded because the near-surface conditions at the surface wave exploration location were different to those at HUE05.

To know the search ranges for inversion, we made a forward model by referring to the layer depth and V_s

values of a Japan-wide three-dimensional velocity model, the Japan Seismic Hazard Information Station version 2 model (J-SHIS V2; Fujiwara et al. 2012; NIED 2019c) and Takai et al. (2019) before estimating the shallow V_s structure at HUE01 and HUE05. The search range for the inversion is shown in Table 2. The V_s value for the shallowest layer was determined from the observed phase velocities in the high-frequency range. At HUE01 and HUE05, the V_s values of 1.3 km/s or below and the value of 1.7 km/s were taken from Takai et al. (2019) and J-SHIS V2 model, respectively. We additionally inserted the 1.0 km/s layer reported by Hatayama et al. (2007) at HUE05. We estimated the shallow V_s structure at HUE01 and HUE05 by fitting the dispersion curve for the fundamental mode of the Rayleigh waves to the observed phase velocities using a genetic algorithm (GA) inversion method (Yamanaka and Ishida 1996). For this method, the number of generations was 200, the population was 40, the crossover ratio was 70%, and the mutation ratio was 1%. The material density and P-wave velocity for each layer were estimated using the empirical relationship between them and the V_s (Ludwig et al. 1970). The GA was executed 5 times with a randomly selected initial number. The misfit was defined as the average of root means-squares of the differences between the observed

Table 2 Search range used for inversion

Layer no.	HUE01			HUE05		
	V_S (km/s)	Thickness (km)		V_S (km/s)	Thickness (km)	
		Low	High		Low	High
1	0.1200	0.0010	0.0080	0.0990	0.0001	0.0500
2	0.2344	0.0010	0.0300	0.2344	0.0200	0.0800
3	0.4000	0.0100	0.0300	0.4000	0.0010	0.1000
4	0.5000	0.0100	0.0450	0.5000	0.0010	0.1000
5	0.7800	0.0100	0.5000	0.7800	0.0100	0.3000
6	–	–	–	1.0000	0.3000	1.5000
7	1.3000	0.0100	1.0000	1.3000	0.3000	1.5000
8	1.7000	∞		1.7000	∞	

and theoretical phase velocities. The solution with the lowest misfit value was selected as the best solution. The observed phase velocities and the theoretical dispersion curve for the estimated V_S structures are compared in Fig. 3. The theoretical dispersion curve explains well the observed phase velocities in the ranges of 0.8–30 Hz and 0.7–7 Hz at HUE01 and HUE05, respectively. The variability of each V_S structure estimated by the GA inversions was small for the search range. The phase velocities at HUE04 and HKD126 are also shown in Fig. 3.

Deep S-wave velocity structures

Takai et al. (2019) did not discuss the deep V_S structures in detail and there are significant differences between the detected V_S structures and the J-SHIS V2 model. One reason for these differences is that the phase velocities obtained from microtremor array observations in the low-frequency range were for a higher-mode despite the fundamental mode assumption, so the deep V_S structures were estimated at a depth that was shallower than the actual depth. Several previous studies have reported that higher-mode phase velocities contributed to observed

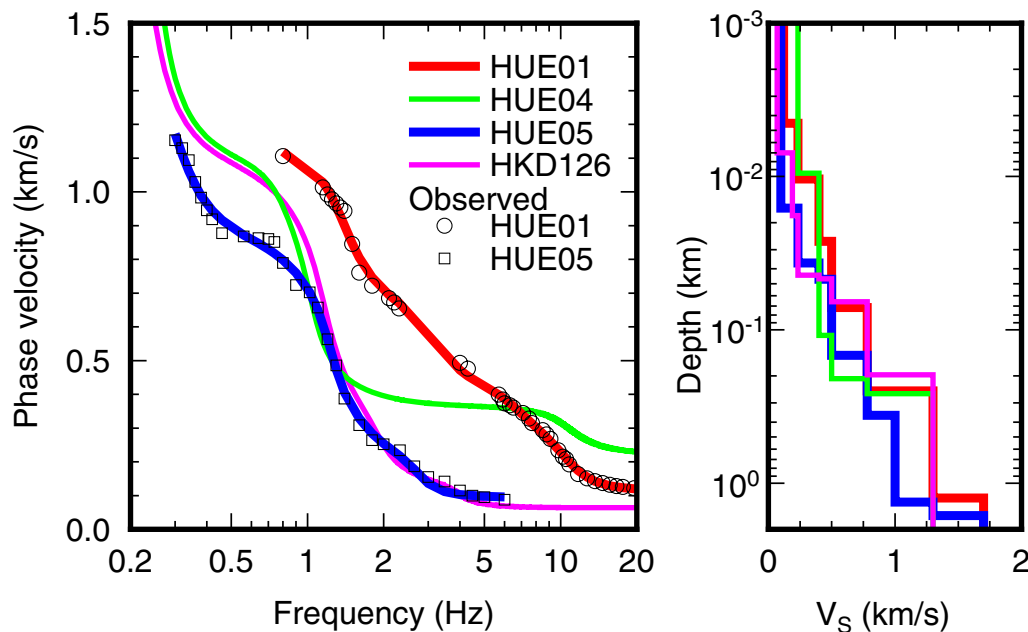


Fig. 3 Phase velocities of the Rayleigh waves and S-wave velocity structure. The circles and rectangles indicate the observed phase velocities obtained using the SPAC and MASW methods at HUE01 and HUE05, respectively. The solid lines indicate the theoretical phase velocity for the estimated V_S structure obtained using the SPAC and MASW methods. The red, green, blue, and magenta lines indicate HUE01, HUE04, HUE05, and HKD126, respectively

phase velocities in microtremor array observations (e.g., Ohori et al. 2002; Köhler et al. 2007). Higher-mode phase velocities in the low-frequency range have been observed in the eastern part of the Yufutsu Plain (e.g., Kunimatsu et al. 2005).

Based on seismic interferometry, ACF analysis has recently been applied to seismic waveforms to estimate layer boundaries beneath a single strong-motion station. ACF analysis using P-waves from teleseismic data was used to estimate the depth of the ice-rock interface and the Moho discontinuity (e.g., Phạm and Tkalčić 2017, 2018). ACF analysis using strong-motion data was also used to tune the depth of the seismic bedrock by fitting the theoretical ACF to the linear-stacked ACF (e.g., Chimoto and Yamanaka 2020).

To tune the deep V_S structures, we performed an ACF analysis using strong-motion data at the four stations. We assumed that the initial velocity structures (model 1) were a combination of the detected shallow structures and the J-SHIS V2 model at HUE01 and HUE05. Those at HKD126 and HUE04 were based on the detected structures reported by Takai et al. (2019). An attenuation was assumed to be $Q=0.1V_S$ km/s.

To verify and tune the deep V_S structures at the four stations, we performed an ACF analysis. We used small-magnitude ($M1.0-6.0$ and depth <50 km determined by Katsumata et al. 2019) strong-motion records at three temporary stations as shown in Fig. 1a. Because the number of events recorded at HKD126 was small, we used all the strong-motion records (Fig. 1a). Table 1 shows the number of events recorded at each station and used for the ACF analysis. The data processing for ACF analysis was as follows. We extracted strong-motion data with a duration of 60 s including P- and S-waves (Chimoto and Yamanaka 2019), and selected the low-noise data, which was the S-wave part could be recognized by visual inspection among the extracted 60 s records. The mean value was removed from the raw acceleration waveform and the horizontal components were rotated to the radial and transverse components. The transverse component was used in subsequent analyses because we assumed the ACF for SH waves. We performed a fast Fourier transform (FFT) after applying a 5% cosine taper to the waveform. The smoothed spectrum was calculated using the Parzen window. Then, the whitened spectrum was calculated by dividing the raw Fourier spectrum by its smoothed spectrum, and the ACF was calculated by applying the inverse FFT to the whitened spectrum after band-pass filtering. The linear-stacked ACF for each event was the final ACF. To make the signal of the final ACF clear, we also used the phase-weighted stack (PWS) method (Schimmel and Paulssen 1997), which can effectively reduce noise in stacking results. Considering the

influence on the peak and trough amplitude of ACFs, the following parameters for ACF analysis were determined by trial and error: the band-pass filter was 1.8–4.2 Hz at HUE01 and HUE04 and 0.5–2.0 Hz at HUE05 and HKD126, and the smoothing bandwidth was 1.0 Hz. In addition, we defined epicentral distance-to-depth ratios as an apparent angle of incidence and used strong-motion data with the apparent angle of incidence of less than 30 degrees (the arctangent of the ratio is less than 0.5774) at the temporary stations under the assumption of vertical incidence.

Autocorrelation function analysis

Figure 4 shows the ACF for each event sorted by the back azimuth at HUE04 as an example. The PWS and linear-stacked ACFs are also shown. Common troughs appear for the ACFs near times of 0.95 and 1.75 s. Clear troughs were confirmed in the linear-stacked ACF and PWS ACF. However, the northeast-to-south event (No. 230–480) has a trough of around 2.0 s, with no troughs in other

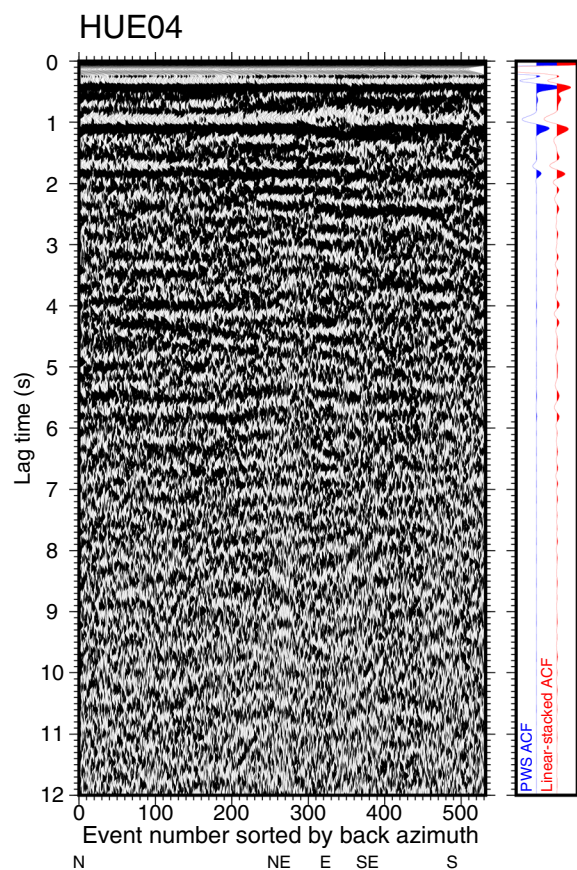


Fig. 4 ACFs, PWS and linear-stacked ACFs at HUE04. The left panel shows the ACF for each event and the right panel shows the corresponding PWS (blue) and linear-stacked (red) ACFs. The event number is sorted by the back azimuth. N, NE, E, SE, and S indicate north, northeast, east, southeast, and south, respectively

directions. The ACF for each event from the north to the northeast (No. 0–270) has a trough of around 4.2 and 5.6 s. On the other hand, the ACF for each event from the southeast to the south (No. 380–530) has troughs around 3.9 and 5.1 s. It can be seen that different back azimuths result in different trough locations for the ACF. For the linear-stacked and PWS ACFs, the trough locations match up to 2.0 s. Some peaks and troughs have very small amplitudes after 2.0 s for the PWS ACF, even though there are some peaks and troughs for each ACF in the local back azimuth range. It seems that the linear-stacked ACF in the whole back azimuth is unsuitable for this site.

To confirm the difference in the locations of troughs in the ACFs in the local back azimuth, we calculated the PWS ACFs for each back azimuth range. Figure 5 shows the PWS ACF, the number of events, and the average apparent angle of incidence of the events, for each back azimuth. The PWS ACFs were calculated when there were more than five records within ± 10 degrees per

degree in back azimuth, allowing for overlap. The PWS ACF was multiplied by a constant to increase its amplitude after 2.0 s. It was confirmed that the locations of the troughs changed depending on the back azimuth. Furthermore, it was found that the clarity of the signal differs greatly after 3.0 s, which corresponds to reflected waves from the deep layer depending on the back azimuth. At HUE01, the troughs at 5.9 s from the northeast to the east appear earlier toward the north where the apparent angle of incidence increases. At HUE04, continuous troughs appear at 2.0–3.0 s on the east side where the apparent angle of incidence is small, and the signals after 3.0 s are clearer than those in other back azimuths. At HUE05, it was found that the trough locations on the east side were very different from those on the north side. On the east side, it was also found that the locations of the troughs were different at the east–southeast boundary after 4.5 s. At HKD126, clear troughs appeared around 2.8 s on the north side, and gradually change toward the south side. A trough was confirmed at 5.0 s on the north side and at

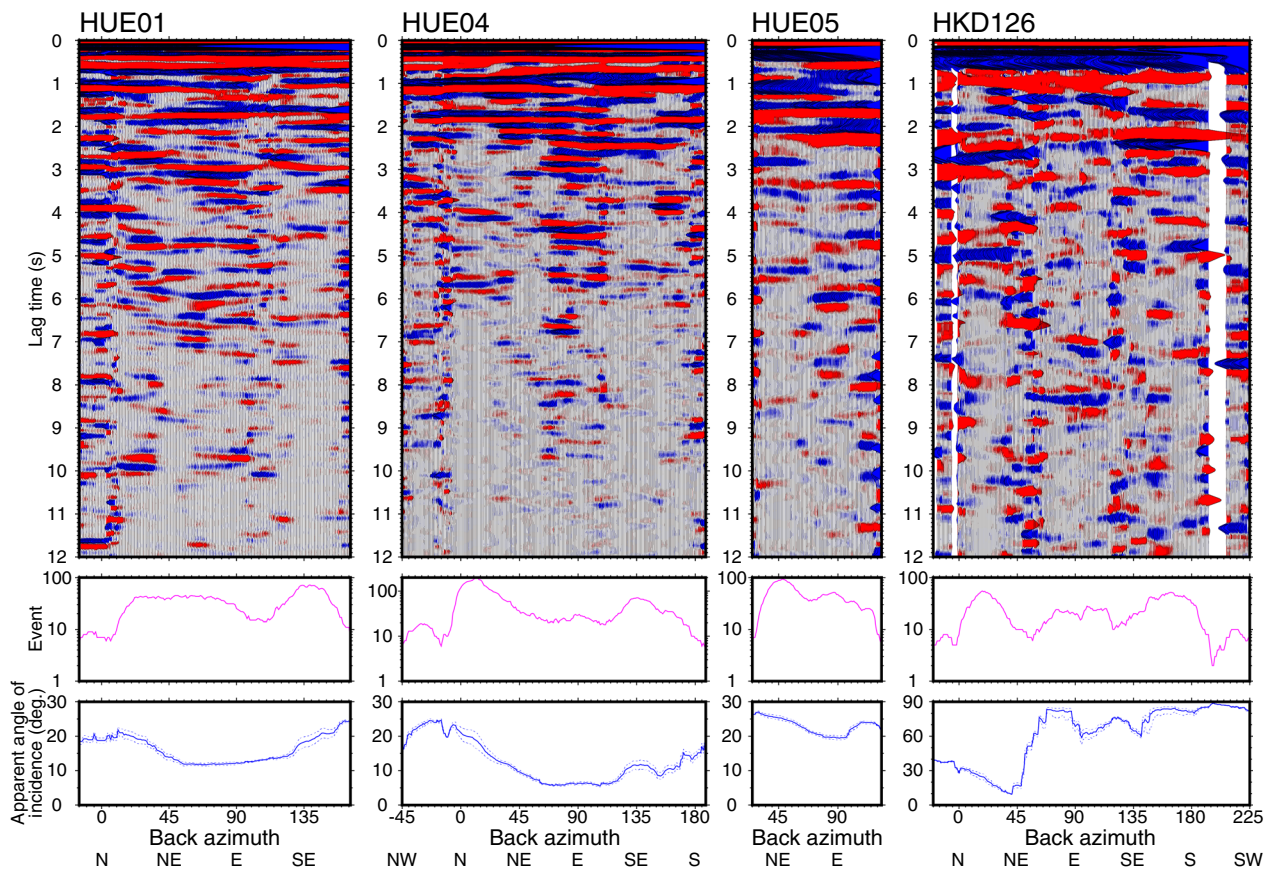


Fig. 5 PWS ACFs for each back azimuth. The top panels show the PWS ACF at each back azimuth. The blue and red indicate trough and peak, respectively. The PWS ACFs were calculated when there were more than five records within ± 10 degrees. The two panels show, from top to bottom, the number of events used for PWS ACF (magenta), and the arctangent of the ratio of epicenter distance to hypocenter depth (blue). Solid lines represent mean values and dashed lines represent \pm one standard deviation from the average. NW, N, NE, E, SE, S and SW indicate northwest, north, northeast, east, southeast, south, and southwest, respectively

8.3 s on the east side. The deep V_S structures were tuned using records in the range where the apparent angle of incidence was small and the trough was visible.

Tuning of S-wave velocity structures using ACF

We created model 2 by modifying the layer boundaries of model 1 such that the troughs and peaks of the theoretical ACF matched those of the PWS ACFs. The theoretical ACFs were calculated by assuming SH wave incident vertically on the layered structure based on Nakahara (2006). Attenuation was assumed to be $Q=0.1 V_S$ km/s. The PWS ACFs used for tuning were calculated using the following records: the northeast to the east–north-east records (from 45 to 100 degrees, 110 records) for HUE01, the northeast to the southeast records (from 40 to 130 degrees, 129 records) for HUE04, the east records (from 80 to 105 degrees, 29 records) for HUE05, and the

north to the northeast records (from 0 to 35 degrees, 60 records) for HKD126. Figure 6 shows the PWS ACFs and the theoretical ACFs calculated using model 1. The PWS ACFs were multiplied by a constant to amplify the peaks and troughs after 4.0 s. We found troughs with the PWS ACF at each station, as shown in Fig. 6. After 2.0 s, the trough locations for the theoretical ACFs differ from those for the PWS ACFs at the four stations.

We tuned the deep V_S structures at the four stations. We inserted a 2.7 km/s layer that is not in the J-SHIS V2 model at HUE05 to explain the trough at 7.5 s. At HUE04 and HKD126, we took the velocity values from the J-SHIS V2 model more than V_S 1.7 km/s to create model 2. In the plain area at HKD126, a layer with a V_S of 1.0 km/s was inserted to explain the 2.0 s trough of the PWS ACF.

We tuned manually the depth of the layers V_S of above 1.0 km/s to fit the theoretical peaks and PWS ACFs.

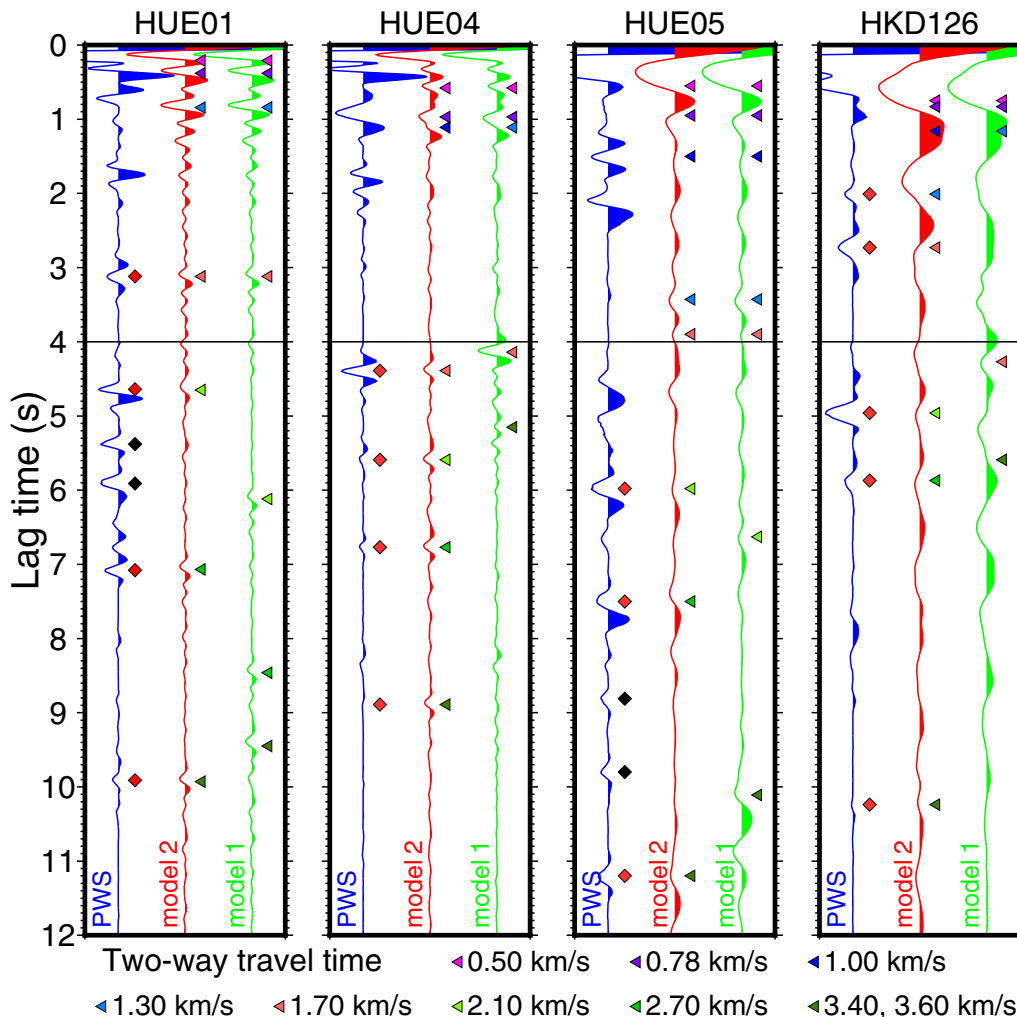


Fig. 6 PWS and theoretical ACFs at four stations. The PWS ACF after 4.0 s was multiplied by six at HUE01 and HUE04, and three at HUE05 and HKD126. Triangles represent the two-way travel time for each layer boundary and diamonds indicate the trough locations in the PWS ACF. The red diamond is the trough used for tuning

For example, at HUE01, there are many clear troughs at 4.6–7.1 s, so the theoretical ACF troughs were matched to the PWS ACF troughs by tuning the layer boundary by trial and error. We assumed that the large trough at 4.6 s corresponds to the 2.1 km/s layer boundary and that the trough at 7.1 s corresponds to the 2.7 km/s layer boundary. The theoretical ACFs obtained using the tuned structures (model 2) fit the PWS ACFs better than the theoretical ACFs with model 1 (Fig. 6).

We compared model 2, which was tuned based on ACF analysis, with the existing structures and model 1. Figure 7 shows the V_S structure at each station. The most remarkable result of the tuning is that the depths for a V_S of more than 2.7 km/s for model 2 at HKD126 and HUE04 are more than twice as deep as those for model 1.

Discussion

We tried to simulate a small earthquake with a one-dimensional V_S structure at each site (Fig. 7) to verify the obtained structures. The target earthquake was that which occurred at 9:48 JST (UTC + 9), September 14, 2018. The seismic moment was 2.04×10^{15} Nm and the hypocenter depth was 36 km (M_w 4.2). The focal mechanism for this earthquake by NIED F-net (NIED 2019a) is shown in Fig. 1a. We inserted Japan Integrated Velocity Structure Model (JIVSM; Koketsu et al. 2012) below the seismic bedrock (V_S of 3.4–4.5 km/s) into both models. We assumed a horizontal multilayered medium

below each station in the simulation and used the discrete wavenumber method (Takeo 1985). The P-wave velocities and densities were calculated by the empirical relationship with the V_S from Ludwig et al. (1970). The source time function had a bell shape with a pulse width of 0.55 s, as determined by trial and error to fit the pulse width at HUE01. Figure 8 shows the synthesized and observed waveforms at each station. To remove errors in the origin time of the earthquake and confirm the relative S-wave initial motion through the sedimentary layers, all-synthesized velocity waveforms were shifted manually by the same time-shift value. The value was determined so that the synthesized initial motion of the S-wave corresponded to the observed one at HUE04. As a result of the simulation, the relative S-wave initial motion of the waveforms synthesized using model 1 arrive at HKD126 about 0.5 s earlier and at HUE01 and HUE05 about 1.4 s later than the observed ones. In model 2 tuned based on the ACF analysis, the layer boundary depth of the V_S of above 2.7 km/s was twice deeper than that in model 1 at HKD126 and HUE04. Since several layers were inserted between V_S 0.78 and 2.7 km/s, the relative theoretical travel time does not become much late compared with that of model 1. The synthesized waveforms calculated with models 1 and 2 are almost the same around the direct S-wave because the amplification is mainly controlled by the shallow structure of V_S of above 1.7 km/s. On the other hand, the later phases of the synthesized

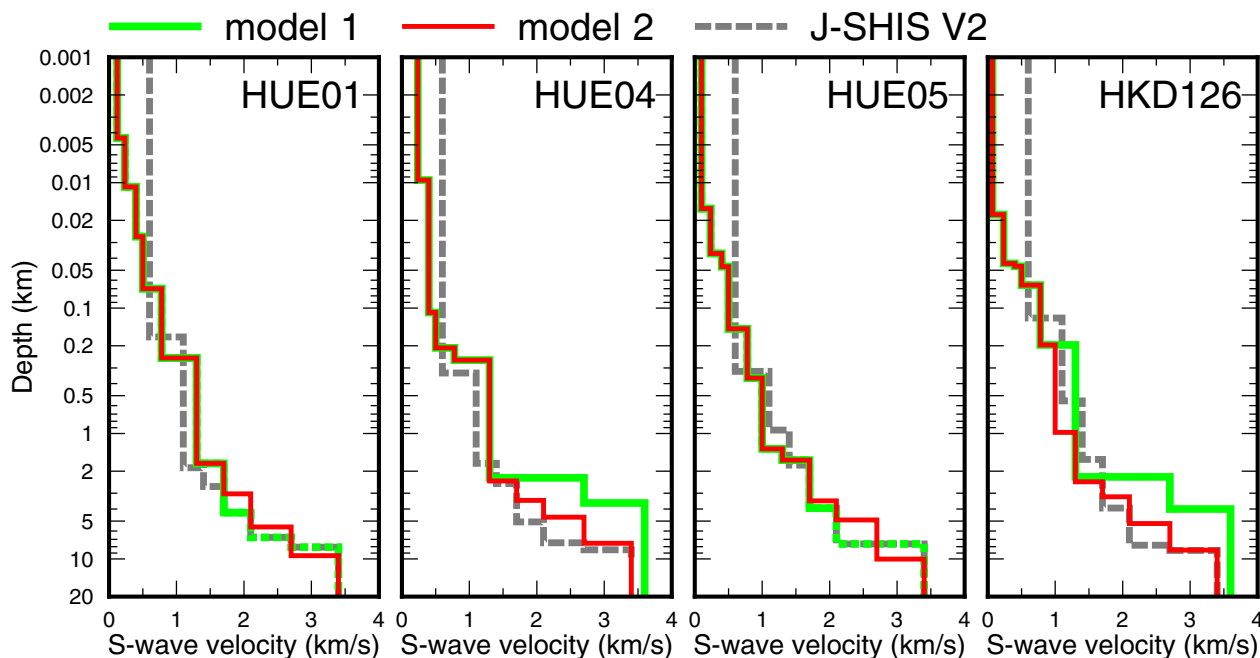


Fig. 7 Estimated S-wave velocity structures at four stations. The green and red lines indicate model 1 and model 2, respectively. The gray dashed line indicates the J-SHIS V2 model

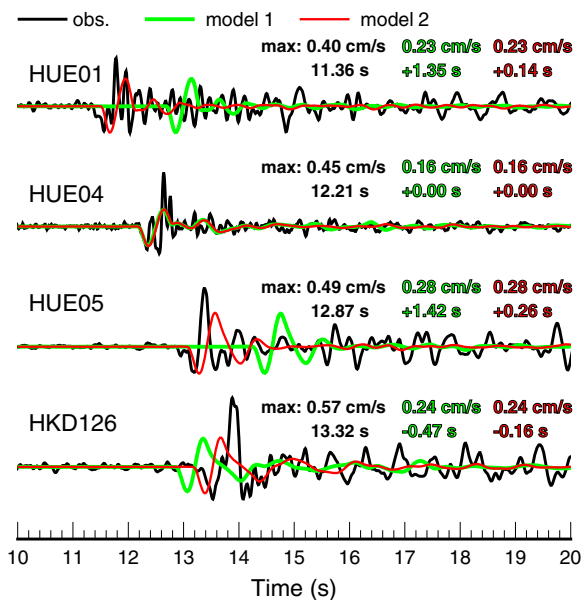


Fig. 8 Comparison of velocity waveforms for the event at 9:48 JST September 14, 2018, M_w 4.2. The black line indicates the observed waveform. The green and red lines are the synthesized waveforms obtained using the structure in model 1 and in this study (model 2), respectively. These models inserted JIVSM (V_S of 3.4–4.5 km/s) below the seismic bedrock. The values with unit cm/s for each color on the graph represent the peak ground velocity for that color waveform. The black value with unit s represents the lag time of the S-wave initial motion of the observed records and the green and red ones represent the time differences between the observed and synthesized S-wave initial motion

waveforms are different due to the multiple reflections from the deep layer boundary. The relative S-wave initiation of the synthesized waveforms, which was manually

shifted by 1.72 s earlier, calculated by the discrete wave-number method with the same parameters except for V_S structures was greatly improved at all stations.

We also compared the theoretical travel time difference with the observed arrival time difference, including at the hypocenter locations not used in the ACF analysis. Assuming that the V_S structure below each station is a horizontal multilayered medium combined with JIVSM under a seismic bedrock, the theoretical travel time was calculated from the layer where the hypocenter was located as follows. We calculated the length of the shortest seismic ray from the hypocenter to the station at each layer according to Snell’s law. Then, the theoretical travel time was obtained by summing the time, which was calculated by dividing the length by the V_S , required to pass through each layer. The observed arrival time difference and theoretical travel time difference were calculated using the records as shown in Fig. 1a and Table 1. We picked the S-wave initial motions of the observed records. The observed arrival time difference was obtained by subtracting the arrival time of the S-wave at HUE04 as a reference from that of the S-wave at other stations. The theoretical travel time difference was calculated by subtracting the theoretical travel time of the S-wave of the synthesized waveform of the reference site from that of the synthesized one of the other sites for each model. The reason HUE04 was used as a reference for each model was that its waveforms for the PWS ACF and theoretical ACFs were more similar than those for other stations. Figure 9 compares the theoretical and observed time differences. The theoretical travel time differences for model 2 are significantly improved compared to those for model 1. The varieties of the theoretical travel times are smaller than the observed ones at

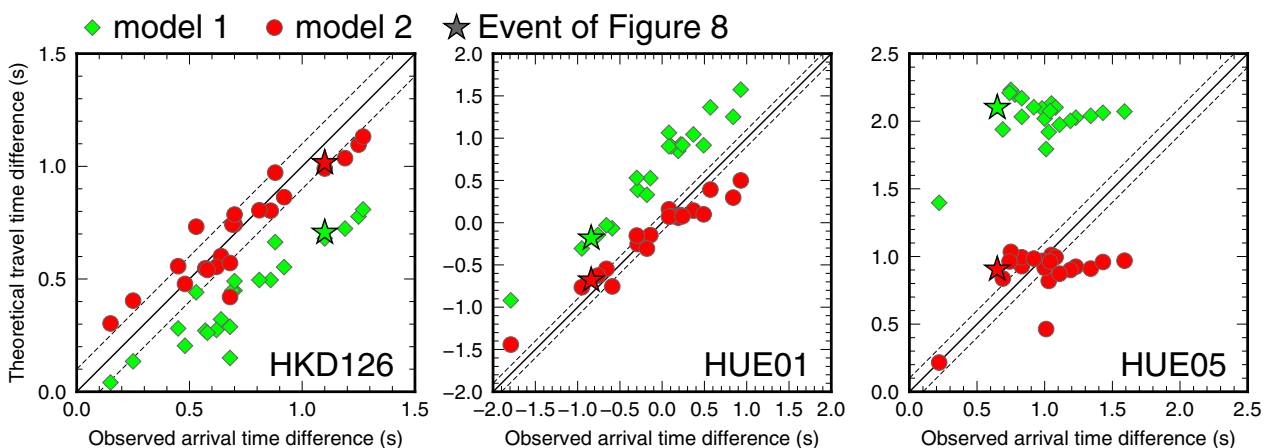


Fig. 9 Observed S-wave arrival time difference and theoretical travel time difference for each event. The green diamonds indicate time differences calculated using model 1. The red circles indicate the time differences calculated using model 2. The red and green stars indicate the time differences of the event in Fig. 8. Both models include JIVSM under the seismic bedrock. The solid line indicates where the two differences between the observed arrival time difference and the theoretical travel time difference match, and the dashed lines are ± 0.1 s away from the solid line

HUE05. One of the reasons is that the condition of the calculation assumes a horizontal multilayered medium. The inclined layer boundaries around the basin edge were estimated (e.g., Yoshida et al. 2007; NIED 2019c), and HUE05 was farther from the basin edge than other stations. Therefore, the observed arrival time differences have varieties.

Since the validity of model 2 was confirmed using S-wave initial motion, we compared the layer boundary depths for model 2 among stations. In model 2, the depth of the seismic bedrock is about 7 km at HUE04, which is the shallowest of the four stations, and deeper than 10 km at HUE05. The site with the deepest seismic bedrock is HUE05. In several previous studies, the seismic bedrock in the Yufutsu Plain has been estimated around 8–10 km (e.g., Iwasaki et al. 2019; Yoshida et al. 2022). We consider the depth of the seismic bedrock for model 2 to be reasonable from these studies. Since the target area is located on the west side of the Hidaka arc–arc collision zone, the depth of the seismic bedrock was complex (Iwasaki et al. 2004). The depth of the seismic bedrock at HUE05 was more deeply estimated by 3 km than that at HUE04. The complexity of the V_S structure is considered to be one of the factors for this difference in the seismic bedrock depth in the plain. The difference is reasonable, even though it is reversed from the J-SHIS V2 model, because HUE05 was located closest to the center of the basin.

Verification and tuning of the three-dimensional V_S structure model are essential for ground-motion prediction. The three-dimensional V_S structure models have been confirmed and modified using many stations by assuming one-dimensional V_S structures (e.g., Wakai et al. 2019; Zhu et al. 2019; Asano et al. 2022). Chimoto and Yamanaka (2020) conducted an ACF analysis in the Kanto Plain, which has little undulation bedrock, and the V_S structure has been tuned from the lag time of the clear trough of the ACF. We also tuned deep V_S structures in the Yufutsu plain, which has complex V_S structures, by ACF analysis using records of specific azimuth assuming a horizontal multilayered medium. As shown in the ACF of each event (Fig. 5), the lag time of the trough differently appeared depending on the back azimuth. The lag time difference was considered to be due to the topological bedrock undulations. It has the potential to detect the inclination of the bedrock and will be useful information for the interpolation of the three-dimensional V_S structure model.

The amplitude of the waveform for the theoretical ACFs is different from that for the PWS ACFs (Fig. 6). The reason for this should be discussed based on the attenuation structures in this area and the V_S values.

Concluding remarks

We examined the shallow S-wave velocity structure based on a surface wave exploration, microtremor array observations, and the deep S-wave velocity structures using an ACF analysis at four stations in the eastern part of the Yufutsu Plain. The deepest seismic bedrock was identified at the site closest to the center of the basin. The deep V_S structure layer boundaries were tuned to be deeper than those estimated based on large-sized microtremor array observations. Based on the ACF analysis, the seismic bedrock depths are around 7 to 10 km in the eastern part of the Yufutsu Plain. We verified the tuned structures by comparing simulation waveforms with tuned models and observed waveforms. The differences in the observed arrival time could be explained by differences in the theoretical travel time calculated using V_S structures tuned based on ACF analysis. According to the ACF analysis, the arrival times of the peaks and troughs are strongly affected by the back azimuth. This suggests that bedrock undulations can be detected based on ACF shape differences classifying the back azimuth. In future studies, we will classify the hypocenter distribution, determine the relationship with the reflected wave arrival time of the ACF, and examine the detailed topological bedrock undulations. In addition, we will examine the attenuation structure using the amplitude of ACF analysis in detail, and the waveform of the later phase and peak ground velocity will be reproduced using the three-dimensional finite difference method.

Abbreviations

ACF	Autocorrelation function
FFT	Fast Fourier transform
JIVSM	Japan Integrated Velocity Structure Model
JMA	Japan Meteorological Agency
J-SHIS	Japan Seismic Hazard Information Station
JST	Japan Standard Time
K-NET	Kyoshin network
M_w	Moment magnitude
NIED	National Research Institute for Earth Science and Disaster Resilience
PWS	Phase-weighted stack
SPAC	Spatial autocorrelation
UTC	Coordinated Universal Time
V_S	S-wave velocity

Acknowledgements

We thank the Japan Meteorological Agency (JMA) and National Research Institute for Earth Science and Disaster Resilience (NIED) for providing us with hypocenter information, strong-motion data, and S-wave velocity structures. We used the Generic Mapping Tools (Wessel et al. 2019) for drawing all of figures. We also thank Mr. Masayoshi Ichiyonagi for providing the hypocenter information. We appreciate the Guest Editor, Dr. Fabrice Cotton, and two anonymous reviewers for their constructive comments, which improved the manuscript significantly.

Author contributions

All authors designed this study. NN planned the microtremor and MASW measurements. NT and MS planned the temporary strong-motion

observations. NN drafted the manuscript. All authors read and approved the final manuscript.

Funding

This study was supported in part by the Japan Society for the Promotion of Science (JSPS) KAKENHI Grant numbers JP20H00268 and JP22H00234, the Ministry of Education, Culture, Sports, Science and Technology (MEXT) of Japan, under its Earthquake, Volcano Hazards Observation and Research Program, the Obayashi Foundation, and JST under the Establishment of University Fellowships towards the Creation of Science Technology Innovation Grant number JPMJFS2101.

Availability of data and materials

The temporary strong-motion data used in this study can be obtained from the corresponding author upon reasonable request. The strong-motion waveform data from K-NET (Aoi et al. 2020; NIED 2019b) were provided by NIED via their website (<https://www.kyoshin.bosai.go.jp/>). The NIED F-net moment tensor catalog (NIED 2019a) is open to the public at <https://www.fnet.bosai.go.jp/top.php?LANG=en>. The J-SHIS V2 model (NIED 2019c) was downloaded from the NIED J-SHIS website at <https://www.j-shis.bosai.go.jp/en/>.

Declarations

Ethics approval and consent to participate

Not applicable.

Consent for publication

Not applicable.

Competing interests

The authors declare that they have no competing interests.

Author details

¹Hokkaido University, Kita 13, Nishi 8, Kita-ku, Sapporo, Hokkaido, Japan.

²Kyushu University, Motoooka 744, Nishi-ku, Fukuoka, Japan.

Received: 1 November 2022 Accepted: 7 March 2023

Published online: 22 March 2023

References

- Aoi S, Asano Y, Kunugi T, Kimura T, Uehira K, Takahashi N, Ueda H, Shiomi K, Matsumoto T, Fujiwara H (2020) MOWLAS: NIED observation network for earthquake, tsunami and volcano. *Earth Planets Space* 72:126. <https://doi.org/10.1186/s40623-020-01250-x>
- Asano K, Iwata T, Yoshida K, Inoue N, Somei K, Miyakoshi K, Ohori M (2022) Microtremor array surveys and development of the velocity model in the Hakodate Plain, Hokkaido, Japan. *Earth Planets Space* 74:94. <https://doi.org/10.1186/s40623-022-01647-w>
- Chimoto K, Yamanaka H (2019) S-Wave velocity structure exploration of sedimentary layers using seismic interferometry on strong motion records. *Explor Geophys* 50:625–633. <https://doi.org/10.1080/08123985.2019.1654835>
- Chimoto K, Yamanaka H (2020) Tuning S-wave velocity structure of deep sedimentary layers in the Shimousa region of the Kanto basin, Japan, using autocorrelation of strong-motion records. *Bull Seismol Soc Am* 110:2882–2891. <https://doi.org/10.1785/0120200156>
- Dziewonski A, Bloch S, Landisman M (1969) A technique for the analysis of transient seismic signals. *Bull Seismol Soc Am* 59:427–444. <https://doi.org/10.1785/bssa0590010427>
- Fujiwara H, Kawai S, Aoi S, Morikawa N, Senna S, Azuma H, Ooi M, Hao KX, Hasegawa N, Maeda T, Iwaki A, Wakamatsu K, Imoto M, Okumura T, Matsuyama H, Narita A (2012) Some improvements of seismic hazard assessment based on the 2011 Tohoku Earthquake. Technical note of the National Research Institute for Earth Science and Disaster Prevention 379. <https://doi.org/10.24732/nied.00001993>
- Hatayama K (2008) Lessons from the 2003 Tokachi-oki, Japan, earthquake for prediction of long-period strong ground motions and sloshing damage to oil storage tanks. *J Seismol* 12:255–263. <https://doi.org/10.1007/s10950-007-9066-y>
- Hatayama K, Kanno T, Kudo K (2007) Control factors of spatial variation of long-period strong ground motions in the Yufutsu sedimentary Basin, Hokkaido, during the Mw 8.0 2003 Tokachi-oki, Japan. *Earthquake Bull Seismol Soc Am* 97:1308–1323. <https://doi.org/10.1785/0120060200>
- Ikeda K, Hasaka T, Murase T (1995) Holocene sediments and topography of the Yufutsu plain in Hokkaido. *Bull Geol Surv Jpn* 46:283–300
- Iwasaki T, Adachi K, Moriya T, Miyamachi H, Matsushima T, Miyashita K, Takeda T, Taira T, Yamada T, Ohtake K (2004) Upper and middle crustal deformation of an arc–arc collision across Hokkaido, Japan, inferred from seismic refraction/wide-angle reflection experiments. *Tectonophysics* 388:59–73. <https://doi.org/10.1016/j.tecto.2004.03.025>
- Iwasaki T, Tsumura N, Ito T, Arita K, Matsubara M, Sato H, Kurashimo E, Hirata N, Abe S, Noda K, Fujiwara A, Kikuchi S, Suzuki K (2019) Structural heterogeneity in and around the fold-and-thrust belt of the Hidaka Collision zone, Hokkaido, Japan and its relationship to the aftershock activity of the 2018 Hokkaido Eastern Iburu Earthquake. *Earth Planets Space* 71(1):103. <https://doi.org/10.1186/s40623-019-1081-z>
- Katsumata K, Ichiyanagi M, Ohzono M, Aoyama H, Tanaka R, Takada M, Yamaguchi T, Okada K, Takahashi H, Sakai S, Matsumoto S, Okada T, Matsuzawa T, Hirano S, Terakawa T, Horikawa S, Kosuga M, Katao H, Iio Y, Nagaoka A, Tsumura N, Ueno T, The Group for the Aftershock Observations of the 2018 Hokkaido Eastern Iburu Earthquake (2019) The 2018 Hokkaido Eastern Iburu earthquake (MJMA = 6.7) was triggered by a strike-slip faulting in a stepover segment: insights from the aftershock distribution and the focal mechanism solution of the main shock. *Earth Planets Space* 71:53. <https://doi.org/10.1186/s40623-019-1032-8>
- Köhler A, Ohnberger M, Scherbaum F, Wathelet M, Cornou C (2007) Assessing the reliability of the modified three-component spatial autocorrelation technique. *Geophys J Int* 168(2):779–796. <https://doi.org/10.1111/j.1365-246X.2006.03253.x>
- Koketsu K, Miyake H, Suzuki H (2012) Japan integrated velocity structure model version 1. In: Proceedings of the 15th world conference on earthquake engineering, Lisbon, 24–28 September 2012.
- Kudo K, Kanno T, Okada H, Özel O, Erdik M, Sasatani T, Higashi S, Takahashi M, Yoshida K (2002) Site-specific issues for strong ground motions during the Kocaeli, Turkey, earthquake of 17 August 1999, as inferred from array observations of microtremors and aftershocks. *Bull Seismol Soc Am* 92:448–465. <https://doi.org/10.1785/0120000812>
- Kunimatsu S, Yoshimi M, Sekiguchi H, Horikawa H, Yoshida K, Saomoto H, Feng S, Sugiyama T (2005) Estimation of subsurface velocity structure under Yufutsu Plain by using microtremor array survey. *Annu Rep Active Fault Paleoseismicity Res* 5:1–15
- Lacoss R, Kelly E, Toksöz M (1969) Estimation of seismic noise structure using arrays. *Geophysics* 34:21–38. <https://doi.org/10.1190/1.1439995>
- Ludwig WJ, Nafe JE, Drake CL (1970) Seismic refraction. In: Maxwell AE (ed) *The sea: ideas and observations on progress in the study of the seas*, Part 1, vol 4. Wiley, New York, pp 53–84
- Nakahara H (2006) Theoretical background of retrieving Green's function by cross-correlation: one-dimensional case. *Geophys J Int* 165:719–728. <https://doi.org/10.1111/j.1365-246X.2006.02916.x>
- National Research Institute for Earth Science and Disaster Resilience (2019a) NIED F-net. National Research Institute for Earth Science and Disaster Resilience, Tsukuba. <https://doi.org/10.17598/nied.0005>
- National Research Institute for Earth Science and Disaster Resilience (2019b) NIED K-NET, KiK-net. National Research Institute for Earth Science and Disaster Resilience, Tsukuba. <https://doi.org/10.17598/nied.0004>
- National Research Institute for Earth Science and Disaster Resilience (2019c) J-SHIS Japan seismic hazard information station. National Research Institute for Earth Science and Disaster Resilience, Tsukuba. <https://doi.org/10.17598/nied.0010>
- Ohori M, Nobata A, Wakamatsu K (2002) A Comparison of ESAC and FK methods of estimating phase velocity using arbitrarily shaped microtremor arrays. *Bull Seismol Soc Am* 92:2323–2332. <https://doi.org/10.1785/0119980109>
- Okada H (2003) The microtremor survey method. Geophysical monograph series, no 12. Society of Exploration Geophysicists, Tulsa. <https://doi.org/10.1190/1.9781560801740>
- Özmen ÖT, Yamanaka H, Alkan MA, Çeken U, Öztürk T, Sezen A (2017) Microtremor array measurements for shallow S-wave profiles at strong-motion

- stations in Hatay and Kahramanmaraş provinces, southern Turkey. *Bull Seismol Soc Am* 107:445–455. <https://doi.org/10.1785/0120160218>
- Park CB, Miller RD, Xia J (1999) Multichannel analysis of surface waves. *Geophysics* 64(3):800–808. <https://doi.org/10.1190/1.1444590>
- Pham T-S, Tkalčić H (2017) On the feasibility and use of teleseismic P wave coda autocorrelation for mapping shallow seismic discontinuities. *J Geophys Res* 122:3776–3791. <https://doi.org/10.1002/2017JB013975>
- Pham T-S, Tkalčić H (2018) Antarctic ice properties revealed from teleseismic P wave coda autocorrelation. *J Geophys Res* 123:7896–7912. <https://doi.org/10.1029/2018JB016115>
- Schimmel M, Paulssen H (1997) Noise reduction and detection of weak, coherent signals through phase-weighted stacks. *Geophys J Int* 130:497–505. <https://doi.org/10.1111/j.1365-246X.1997.tb05664.x>
- Takai N, Shigefuji M, Horita J, Nomoto S, Maeda T, Ichianagi M, Takahashi H, Yamanaka H, Chimoto K, Tsuno S, Korenaga M, Yamada N (2019) Cause of destructive strong ground motion within 1–2 s in Mukawa town during the 2018 Mw 6.6 Hokkaido eastern Iburī earthquake. *Earth Planets Space* 71:67. <https://doi.org/10.1186/s40623-019-1044-4>
- Takeo M (1985) Near-field synthetic seismograms taking into account the effects of anelasticity—the effects of anelastic attenuation on seismograms caused by a sedimentary layer. *Pap Meteorol Geophys* 36:245–257. <https://doi.org/10.2467/mripapers.36.245>
- Tanaka S, Shigefuji M, Kanno T, Takai N (2020) Site amplification characteristics at high seismic intensity strong-motion stations in southwestern epicentral region during the 2018 Hokkaido eastern Iburī earthquake. Summaries of technical papers of annual meeting Architectural Institute Jpn. pp 101–102
- Wakai A, Senna S, Jin K, Yatagai A, Suzuki H, Inagaki Y, Matsuyama H, Fujiwara H (2019) Modeling of subsurface velocity structures from seismic bedrock to ground surface in the Tokai region, Japan, for broadband strong ground motion prediction. *J Disaster Res* 14:1140–1153. <https://doi.org/10.20965/jdr.2019.p1140>
- Wakamatsu K, Matsuoka M (2020) Update of the nationwide 7.5-arc-second Japan engineering geomorphologic classification map and Vs30 zoning. *Bull Jpn Assoc Earthq Eng* 40:24–27
- Wessel P, Luis JF, Uieda L, Scharroo R, Wobbe F, Smith WHF, Tian D (2019) The generic mapping tools version 6. *Geochem Geophys Geosys* 20:5556–5564. <https://doi.org/10.1029/2019GC008515>
- Yamanaka H, Ishida H (1996) Application of genetic algorithms to an inversion of surface-wave dispersion data. *Bull Seismol Soc Am* 86:436–444. <https://doi.org/10.1785/bssa0860020436>
- Yoshida K, Yoshimi M, Suzuki H, Morino M, Takizawa F, Sekiguchi H, Horikawa H (2007) 3D velocity structure model of the Ishikari and Yufutsu sedimentary basins. *Annu Rep Act Fault Paleoeearthquake Res* 7:1–29
- Yoshida K, Somei K, Miyakoshi K (2022) Estimation of the sedimentary basin structure of the southeastern part of the Ishikari Lowland, Hokkaido, inferred from receiver function. *J Seismol Soc Jpn* 75:145–161. <https://doi.org/10.4294/zisin.2022-1>
- Zhu C, Cotton F, Pilz M (2019) Testing the depths to 1.0 and 2.5 km/s velocity isosurfaces in a velocity model for Japan and implications for ground-motion modeling. *Bull Seismol Soc Am* 109:2710–2721. <https://doi.org/10.1785/0120190016>

Publisher's Note

Springer Nature remains neutral with regard to jurisdictional claims in published maps and institutional affiliations.

Submit your manuscript to a SpringerOpen® journal and benefit from:

- Convenient online submission
- Rigorous peer review
- Open access: articles freely available online
- High visibility within the field
- Retaining the copyright to your article

Submit your next manuscript at ► [springeropen.com](https://www.springeropen.com)
